

Article

Infiltration Response of Adsorbent Amended Filters for Stormwater Management under Freezing/Thawing Conditions

Carlos Monrabal-Martinez ^{*}, Elena Scibilia , Sönke Maus and Tone M. Muthanna 

Department of Civil and Environmental Engineering, Norwegian University of Science and Technology (NTNU), NO-7491 Trondheim, Norway; Elena.scibilia@ntnu.no (E.S.); sonke.maus@ntnu.no (S.M.); tone.muthanna@ntnu.no (T.M.M.)

^{*} Correspondence: carlosmonra84@gmail.com

Received: 15 October 2019; Accepted: 7 December 2019; Published: 12 December 2019



Abstract: Coastal cold climates experience frequent intermittent melting and freezing periods over the cold period. This intermittent freezing in stormwater systems affects the infiltration capacity and hence the performance. This paper investigates the infiltration capacity of engineered filter media (composed of sand mixed with charcoal, pine bark, or olivine) under freezing temperatures in a column-based laboratory setup. Infiltration into partially frozen filter media was replicated using a climate room. The filter media in the columns were brought to $-2.5\text{ }^{\circ}\text{C}$, and water at $+2\text{ }^{\circ}\text{C}$ was percolated through the columns with a constant head of 5 cm. Infiltration performance was assessed by observing the time until breakthrough, and the infiltration rate 24 h after breakthrough. The results were compared to the observed hydraulic conductivity for the unfrozen filter media. A novel approach combining the unfrozen water content curves with X-ray tomographic (XRT) images of the materials was adopted to better understand the thermal and infiltration processes. Breakthrough was observed between ca. 21 and 56 h in all columns. The column with homogeneously mixed filter media with sand yielded the quickest breakthrough. The infiltration rates were higher than recommendations for infiltration-based systems in cold climates, making them a suitable option in cold climates.

Keywords: infiltration performance; stormwater management; cold climate; unfrozen water content; snowmelt

1. Introduction

Infiltration practices have been shown to be an effective solution for retention and infiltration of small to medium storm events [1,2]. Apart from the hydrological benefit of reducing flowrates and total volume, infiltration based systems may enhance the water quality of polluted runoff through sedimentation, filtration, adsorption, and biological processes [3].

Infiltration practices in cold climates face the challenge of low water temperatures in the soil pores. Yet, satisfactory removal of metals, nutrients and sediments have been shown under low temperatures in soil based infiltration systems [4–7]. However, the presence of pore ice has been shown to affect negatively infiltration capacity [8], meaning that the treatment potential regarding water quality is also lowered. This scenario is expected to occur during snowmelt periods, when the ground is still frozen, in which pollutant concentrations in snowmelt runoff generally exceed values observed in rainfall runoff [9,10].

Frozen soil consists of at least five components: mineral grains, organic matter, air, ice, and water. Water can be present as pore fluid (gravitational water), as a film of water weakly bonded to the surface

of solid particles by capillary force (capillary water), as a thin film of strong bonded water (hygroscopic water) held by electrical forces [11]. Hygroscopic water maybe structured with hydrogen bonds (more strongly bonded) or by molecular forces known as osmotic forces (weaker). Unfrozen water is water which can stay liquid in soils below zero degrees Celsius. Fine grain soils always hold unfrozen water due to surface forces between polar water molecules and charged particle surfaces and the ions adsorbed on these surfaces [12]. The presence of unfrozen water in frozen soils was first mentioned by [13] and many different methods have been used since then to obtain freezing characteristic curves of the soil and the temperature; dielectric, nuclear magnetic resonance (NMR), time domain reflectometry, calorimetric, contact, etc. [14–17]. Relationships between unfrozen water content and temperature have been established for many types of soils [18]. The amount of unfrozen water within frozen soils depends on their composition, surface area, structure, and pressure/temperature conditions, and it will impact mechanical and thermal properties of soils [19]. Materials with high unfrozen water content could be an interesting option with regard to ice prevention and, subsequently, water movement through frozen media. This fact motivates research on engineered filter media that can offer better response under freezing conditions.

Diverse methods have been used to quantify and understand infiltration processes in soils subjected to freezing temperatures. Infiltration properties of frozen soils for fuel spills has been tested by a falling head permeameter [20]. Dye tracers has been used to identify meltwater pathways into alpine soils [21]. In order to avoid phase changes due to infiltrating water, [8,22] used an air permeameter to measure infiltration in a frozen sand sample, and the influence of freezing prior to drainage on the infiltration of two typical soils for bio-filtration. Column experiments were performed to examine the effect of the initial soil moisture content prior to freezing and soil temperature on the hydraulic conductivity of a soil used in infiltration based swales, and to study soil thawing processes in two engineered soils designed for bio-filters [23,24]. However, there is a lack of information about unfrozen water content for these stormwater solutions subjected to freezing temperatures.

The National Public Roads Administrator in Norway had an interest in developing filtration based filters with high hydraulic loading capacity for water quality improvements of road runoff. Through a previously published study [25], two filter media had been identified as promising; granular olivine and pine bark. In addition, activated coal was used as a reference based on its known treatment properties. These adsorbent amended filters for treatment of stormwater runoff in cold climate regions allowed water to pass through at high inflow rates while still achieving high metal removal [26]. To improve understanding and knowledge of their suitability in cold climate, the main objectives of this study were; (1) to quantify and explain the impact of pre-freezing water contents on the infiltration capacity of these filters; (2) to investigate the optimal disposition of the adsorbent within the filter with regard to infiltration performance; (3) to investigate the role of the unfrozen water content for infiltration; and (4) to improve the understanding of infiltration and ice content by application of X-ray microtomographic imaging of soils and filters. This combination is a first step in the direction of fundamental modelling of the freeze-thaw processes during percolation of soils and filters.

2. Materials and Methods

2.1. Materials

Three different adsorbents; granulated activated charcoal, olivine in granular form, and pine bark (sieved at <4 mm particle size prior to use) in combination with clean homogeneous sand were tested for infiltration capacity both at room temperature and under freezing/thawing conditions. Relevant mechanical characteristics of the materials used in these filters are shown in Table 1. Particle size distributions were obtained with the sieving method according to [27]. Particle densities (ρ_s , mass of material particles/volume of material particles) were measured with the pycnometer method according to [28] except for pine bark and olivine, which was adopted from [29,30], respectively. Hygroscopic moisture of the materials was measured according to [31]. The particle sizes from 3-d X-ray images

were obtained by a sphere fitting algorithm with the software GeoDict (www.geodict.com). They are thus a measure of the shortest axis length of a 3-d object, while sieving results depend on the two minor dimensions (e.g., sieving would obtain the diameter of a penny, while sphere fitting obtains the thickness). Hence the difference in particles sizes obtained by the methods is related to their shapes deviating from isotropic objects.

Table 1. Material properties of the sand and adsorbents used in the study. Size classes in brackets are obtained from 3-d XRT images.

Parameter	Sand	Olivine	Charcoal	Pine Bark
d_{90}^1 (mm)	0.65 (0.33)	1.9 (1.2)	1.8 (0.77)	(0.72)
d_{60}^1 (mm)	0.40 (0.20)	1.5 (0.89)	1.3 (0.51)	(0.39)
d_{10}^1 (mm)	0.18 (0.07)	0.90 (0.41)	0.7 (0.19)	(0.09)
Uniformity coeff. (d_{60}/d_{10})	2.22 (2.85)	1.66 (2.17)	1.85 (2.68)	(4.33)
ρ_s (g/cm ³)	2.66	3.32	1.91	1.50
ρ_d^2 (g/cm ³)	1.50	1.77	0.53	0.20
η^3 (%)	44	47	72	87
Wsat ⁴ (% by mass)	29.5	24.2	134	446
Whyg (% by mass)	0.06	0.44	4.51	15.4

¹ d_x represents the intercept for x% of the cumulative mass of the particle size distribution. ² Bulk density = ρ_d = mass of material medium/volume of material medium. ³ Porosity = η = volume of pores/volume of sample = $1 - (\rho_d/\rho_s)$. Specific particle gravity = $G_s = \rho_s/\rho_w$, where ρ_w is assumed to be 1 g/cm³. ⁴ Saturated moisture = Wsat = water content when all pores are filled with water (degree of saturation, S_w , is 1) = $\eta \cdot S_r / ((1 - \eta) \cdot G_s)$.

2.2. Methods

In the present study, a column test was performed to simulate freezing/thawing conditions, commonly observed in late winter/early spring in cold coastal climates. A contact method was performed in order to understand the variability of unfrozen water content under freezing temperatures and among materials tested in the columns. In addition, X-ray (Nikon, Tokyo, Japan) micro computed tomography was used in order to understand the composition of the media in the columns, which will help to interpret results from the previous tests.

2.2.1. Column Tests

Plexiglas columns (450 mm long, 100 mm inner diameter, and 5 mm wall thickness) were constructed and used in the study (Figure 1). The column diameter and media diameter ratio was greater than 50, which is recommended for filtration studies [32]. A plastic nozzle (6 mm inner diameter) was embedded in the middle of the bottom lid to convey infiltrated water out of the column. Columns were volumetrically composed of 35 cm sand and 5 cm of adsorbent. The length (40 cm) represents minimum recommended depth for bio-filtration facilities according to recommendations given by [33]. To understand the effect of filter media placement on infiltration capacity, different potential configurations were studied; pine bark was studied at the top and at the bottom of the sand layer, charcoal was studied in the three possible configurations (underlying the sand layer, overlying the sand layer, and homogeneously mixed with sand (Figure 1), and olivine in the homogeneously mixed and the underlying configuration. The volumetric ratio adsorbent to sand was kept constant in all columns regardless of the configuration and filter media.

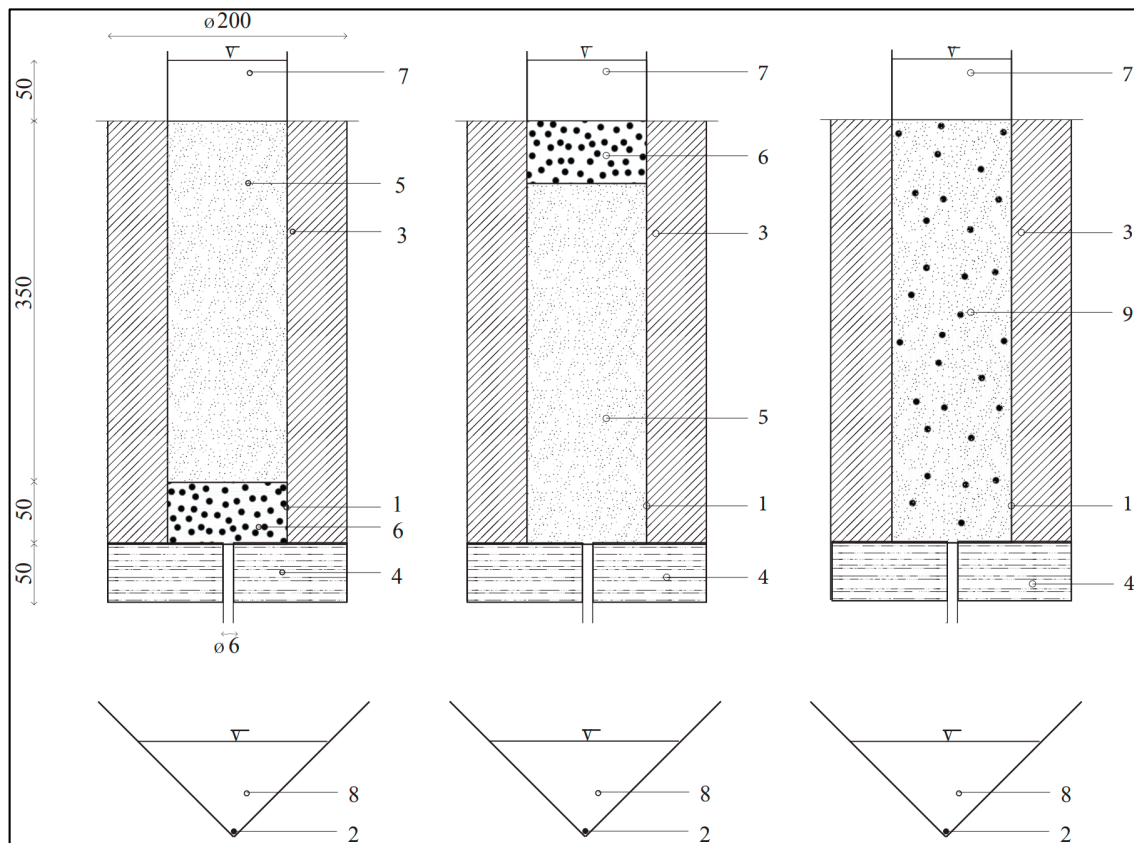


Figure 1. Layout of the column setup used for simulating freezing/thawing conditions. The figure represents the three tested placements of charcoal within the filter, i.e., underlying the sand layer (**left**), overlying the sand layer (**middle**), and homogeneously mixed with the sand (**right**). 1 = thermocouple; 2 = actuator; 3 = lateral insulation; 4 = bottom insulation; 5 = sand; 6 = adsorbent (**charcoal**); 7 = ponding water at $+2 \pm 0.5$ °C; 8 = percolated water; 9 = charcoal mixed homogeneously with sand. Units in mm.

- Infiltration capacity at room temperature

A constant head permeameter based on [34] was modified so it could be applied to the columns. This method was used to evaluate saturated hydraulic conductivity, K_{measured} (mm/s), of the different filters in their respective configurations. Darcy's equation was used to obtain saturated hydraulic conductivities:

$$K_{\text{measured}} = \frac{V \times L}{A \times t \times \Delta h} \quad (1)$$

where V is the volume of water (mL) collected at the outlet, L (mm) is the length between two points in the filter column (h_1 and h_2) with known pressure head, A is the cross section area (mm^2) of the columns, t is the time (seconds) during the water was collected at the outlet, and Δh is the pressure head difference (mm) between P_1 and P_2 .

The saturated hydraulic conductivities, obtained at 20 °C, were adjusted to a temperature of 2 °C (K_2 °C) by using factor of 1.69 based on tables for the dynamic viscosity of water [35]. This allows for comparison with infiltration rates during freezing/thawing conditions.

- Infiltration capacity during freezing/thawing conditions

To evaluate the adverse effects of increasing water content prior to freezing on the potential infiltration capacity the columns described in the previous section were tested with two different initial water contents; (1) fully saturated media (representing, for example, a malfunction drainage that does not allow for draining the media sufficiently quick); (2) water content when the initially saturated media in the column was drained gravitationally for 24 h (representing a field capacity scenario, where the media has drained

out most of the gravitational water). After adjusting the pre-freezing water content, columns were thermally insulated both laterally and underneath by using Climcover Tube Alu2 (thickness = 50 mm and $\lambda = 0.036$ W/(m·K)) and extruded polystyrene Styrofoam 400 SL-A-N (thickness = 50 mm and $\lambda = 0.035$ W/(m·K)), respectively (Figure 1). Columns were introduced into a cold chamber set at -5 °C and the freezing front was assumed to follow a vertical direction downwards. The temperature was monitored inside the columns 2 cm above the bottom of the column by type T thermocouples. Temperature values were registered at 1-minute intervals with a Campbell Scientific CR1000 data logger.

The temperature of the entire column media was brought to -2.5 ± 0.2 °C. To mimic the process of snowmelt infiltration into a partially frozen media, tap water was cooled down to $+2 \pm 0.5$ °C and poured gently on the surface of the column. Lower temperatures of the ponding water would have led to ice formation and pose a complication in terms of reproducibility of the tests. The water level was kept constant at 5 cm above the media and the room temperature was $+2$ °C throughout the duration of the infiltration test.

Two variables, which are of interest for designing infiltration based systems for stormwater control, were measured to evaluate the infiltration response under freezing/thawing conditions. The first variable was the time it took to observe water breakthrough at the outlet, which has been used by other authors to estimate the travel time required for ponding water to infiltrate into and through the depth of the column media [23,24]. This variable was monitored with the help of an actuator that triggered in contact with water. The infiltration rate was measured at 24 h after breakthrough was observed, which is near steady percolation observed by [24]. Therefore, the second variable for evaluating the infiltration response was the decrease in infiltration rate of the partially frozen media with regard to the previously measured $K_{20}^{\circ\text{C}}$. Experiments were triplicated and a control columns (only sand) were used although some columns were disregarded due to leakages that disrupted the results (see Tables 2 and 3).

Table 2. Infiltration parameters obtained during the column tests with saturated media. $K_{20}^{\circ\text{C}}$ and $K_{2}^{\circ\text{C}}$ stands for the corrected saturated hydraulic conductivity at 20 °C and 2 °C, IR for infiltration rate after 24 h since breakthrough and $\text{IR}/K_{2}^{\circ\text{C}}$ represents the decrease in infiltration rate with regard to $K_{2}^{\circ\text{C}}$.

Filter Media	Adsorbent Placement	$K_{20}^{\circ\text{C}}$ ¹ (mm/s)	$K_{2}^{\circ\text{C}}$ ² (mm/s)	Time of Water Breakthrough (h)	IR (mm/s)	$\text{IR}/K_{2}^{\circ\text{C}}$ (%)	Number of Columns
Charcoal and Sand	Overlying	0.17 ± 0.09	0.10 ± 0.05	44.9 ± 5.5	0.018 ± 0.002	18	3
Charcoal and Sand	Mixed	0.19 ± 0.01	0.11 ± 0.01	35 ± 5.2	0.016 ± 0.001	14	2
Charcoal and Sand	Underlying	0.25 ± 0.18	0.15 ± 0.11	51.8 ± 2	0.022 ± 0.001	15	2
Olivine and Sand	Mixed	0.24 ± 0.01	0.14 ± 0.01	34.1 ± 2.7	0.03 ± 0.002	21	2
Olivine and Sand	Underlying	0.34 ± 0.09	0.20 ± 0.05	46 ± 5.3	0.048 ± 0.003	24	3
Pine bark and Sand	Overlying	0.22 ± 0.05	0.13 ± 0.03	46.2 ± 3.9	0.022 ± 0.001	17	3
Pine bark and Sand	Underlying	0.17 ± 0.01	0.10 ± 0.01	55.8 ± 2.2	0.022 ± 0.001	22	2
Sand	-	0.28 ± 0.07 ³	0.17 ± 0.04 ³	50.2 ± 4.5 ³	0.039 ± 0.002 ³	23	1

¹ Obtained by column based laboratory setup experiment. ² Obtained by a constant multiplier of K_{20} (1.69). ³ Average standard deviation based on the deviations obtained during experiments with saturated media.

Table 3. Infiltration parameters obtained during the column tests at field capacity. See Table 2 for abbreviation explanations.

Filter Media	Adsorbent Placement	$K_{20}^{\circ\text{C}}$ ¹ (mm/s)	$K_{2}^{\circ\text{C}}$ ² (mm/s)	Time of Water Breakthrough (h)	IR (mm/s)	$\text{IR}/K_{2}^{\circ\text{C}}$ (%)	Number of Columns
Charcoal and Sand	Overlying	0.21 ± 0.04	0.13 ± 0.02	33.2 ± 1.2	0.014 ± 0.008	11	2
Charcoal and Sand	Mixed	0.21 ± 0.07	0.13 ± 0.04	21.6 ± 2.9	0.008 ± 0.002	6	3
Charcoal and Sand	Underlying	0.24 ± 0.08	0.14 ± 0.05	39.9 ± 3.0	0.017 ± 0.005	12	3
Olivine and Sand	Mixed	0.21 ± 0.07	0.13 ± 0.04	30.9 ± 4.5	0.007 ± 0.001	6	2
Olivine and Sand	Underlying	0.26 ± 0.03	0.16 ± 0.02	33.1 ± 0.7	0.009 ± 0.001	6	2
Pine bark and Sand	Overlying	0.24 ± 0.12	0.14 ± 0.07	37.3 ± 3.3	0.015 ± 0.002	10	3
Pine bark and Sand	Underlying	0.26 ± 0.08	0.16 ± 0.05	49.7 ± 7.8	0.027 ± 0.012	17	2
Sand	-	0.26 ± 0.01	0.16 ± 0.01	41.1 ± 5.8	0.021 ± 0.005	13	2

¹ Obtained by column based laboratory setup experiment. ² Obtained by a constant multiplier of K_{20} (1.69).

2.2.2. Contact Method for Estimation of the Unfrozen Water Content

The sorption method, which is also known as the contact method, was used to estimate the unfrozen water content in the columns. It was developed in the mid-1970s by Russian scientists [14]. This method is based on reaching the thermodynamic equilibrium between ice, unfrozen water, and vapor of initially dry soils in close contact with ice plates. Water uptake in the sample happens through vapor and capillary water transport and stops at the equilibrium point for the amount of unfrozen water at the given negative temperature. The typical contact time needed to reach equilibrium between the dry soils and the ice plates is 1 to 4 days, depending on the soil type.

Unfrozen water content curves were determined for the materials that were part of the stormwater filters as described above; olivine, sand, charcoal and pine bark. In addition, a typical soil for bio-infiltration (70% sand, 24% silt, and 6% clay-loamy sand according to [36], a mix of sand and olivine (in the same proportion as in the column, i.e., 17% by weight, defined as mix 1) and a mix of sand and charcoal (5% by weight, defined as mix 2) were also tested. Before the experiment, all samples were dried at 105 °C for 24 h to remove all hygroscopic water and, subsequently, cooled down to the experimental temperature. Ice lenses of 6 cm diameter and 1 cm thickness were prepared by freezing distilled water in cylinder aluminum cups. Each dry cooled sample was placed between two ice lenses to form a “sandwich” (Figure 2).

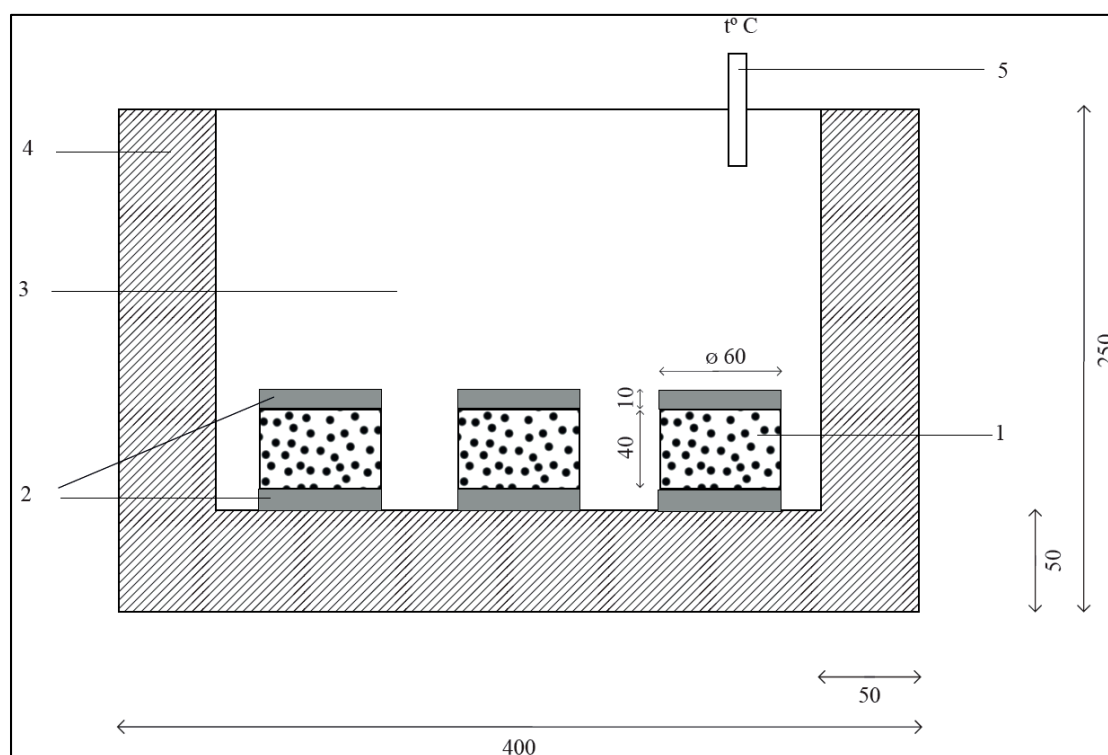


Figure 2. Layout of the contact method setup. 1 = oven-dried sample; 2 = ice lens; 3 = cooling box; 4 = insulation; 5 = thermometer. Units are in mm.

The experiments took place under different temperatures; -2 , -3 , -5 , and -11 °C. After 4 days, materials were pulled out, weighted, and dried at 105 °C for 24 h to calculate the water content by weight. Each water content corresponded to the unfrozen water content at each experimental temperature. Every material was tested in triplicates at each temperature.

The goal of this test was to determine the variability of unfrozen water content under freezing temperatures and among materials tested in the columns. However, unfrozen water only exists in very small pores inside material particles and on their surface since the water in larger pores turns to ice around 0 °C. It is thus not expected to have a large influence on fluid transport at saturation and the

freezing-melting behavior of the related pore space between the particles. To understand the latter part of the pore space, as well as obtain 3-d images of them, a 3-d X-ray microtomography was used, which will be discussed in the next paragraph.

2.2.3. X-Ray Micro Computed Tomography (XRT)

X-ray micro computed tomography (XRT, in medicine best known under the name CT for Computed Tomography) is a non-destructive imaging technique capable of visualizing the internal 3-dimensional structure of an object. During the past decades it has been established as a powerful tool in material and geosciences [37–40]. During XRT a large number of 2-dimensional X-ray transmission images is obtained while a sample is rotating 360° with small increments. From this set of images, a 3-d field of grey values, proportional to the transmission of X-rays, is reconstructed by mathematical algorithms (computed tomography). If the contrast between the materials is large enough, the grey values may be used to distinguish the materials present in the sample. In the present work XRT was applied to visualize the distribution of solid, air and water/ice. Note that the X-ray contrast between liquid water and ice is rather low, and it has not been attempted to resolve it by experiment (it is possible with special contrast-enhancing techniques). However, it was assumed that water in pores larger than 25 micron was frozen by keeping the samples at -2.5°C several days prior to imaging. In what follows, the XRT-derived water content is thus classified as ice.

XRT provides non-destructive 3-d information about the pore space and material distribution in a medium. These virtual images may be used for a detailed grain and pore size analysis as well as numerical simulations of physical properties, e.g., fluid flow simulations to obtain the hydraulic conductivity. The problem of saturation-dependence of physical properties can be addressed. While this has not been done in this present work, it is planned to do so in future studies. The strength of XRT imaging is that the same images may be used for more extensive simulations.

The imaging system allows for a spatial resolution that is approximately 1/2000 of the field of view. Hence there is a trade-off between resolution and sample size. Focusing on fluid flow, it was necessary to choose a spatial resolution (voxel size) of 25 micrometers based on the following considerations for sand. There is a well-defined peak in the pore size distribution at 100–125 micrometer, which means that these pores are sufficiently resolved with the present voxel size. Samples are still large enough to minimize boundary effects and open for future simulation of 3-d freezing. From the pore size distribution it was also deduced that unresolved pores with diameters less than 25 micron are unlikely to increase the pore space by more than a few percent and are not expected to contribute considerably to fluid flow.

It is possible to perform XRT imaging at much higher resolution (nanotomography) to resolve sub-micrometer pores within grains, however this resolution was not accessible by XRT scanner used in this setup (it is accessible at synchrotron facilities). However, it could be asked if this could provide information about pores associated with unfrozen water. Unfrozen water may exist in pores due to surface chemistry/van der Waals forces and not due to the Gibbs–Thomson effect (pore curvature depressing the freezing point). For pure water the diameter of non-freezing pores is typically $0.1/dT$ micrometers, where dT is the supercooling below the freezing point. For the present dT of -2.5 K this implies a pore diameter of 0.04 micrometers for non-freezing pores due to curvature. Surface layers of unfrozen water are likely to have a thickness of the same order of magnitude, far below the XRT resolution used. Hence, there is no overlap between pore sizes imaged by XRT and those related to adsorption of unfrozen water. However, by combining the XRT based porosity measurements with measurements of density and total porosity (based on weighing and solid densities, Table 1) it gives an XRT unresolved porosity that should correspond to the pores and surfaces occupied by unfrozen water plus the regime of pores neither accessible by the unfrozen water nor by the XRT method (0.1–25 micrometer). Conclusions about the consistency of the techniques can be drawn by comparing this unresolved porosity with the independent unfrozen water measurements.

X-ray imaging was performed at the Norwegian Centre of X-ray diffraction and imaging (RECX) at the NTNU in Trondheim, using a XT H 225 ST micro computed tomographic system from Nikon Metrology NV. Operating parameters were a tungsten target, a current source of 260 μA , an acceleration voltage of 175 kV peak, and 3142 rotations per scan. A field of view of 50 mm and a 2000×2000 pixel flat panel detector meant that the unit of graphic information, one pixel, had a size of 25 μm . To keep the samples at the experimental temperature of $-2.5\text{ }^\circ\text{C}$ (as in the column test), a self-assembled thermoelectric cooling stage with top and bottom cooling was used. Samples were scanned in aluminum sample holders with a wall thickness of 1 mm.

After the scanning, the radiographic images were transformed into a 3-d array of grey values by means of reconstruction software from Nikon Metrology NV. The resulting 3-d image consists of 2000^3 voxels with a side length of 25 μm , where each voxel represents a value of the X-ray transmission coefficient. For further analysis and conversion into a 3-d array of phases/materials the freely available ImageJ (rsb.info.nih.gov/ij) software as well as GeoDict (www.geodict.com) for pore space analysis were used. A typical procedure is illustrated based on the horizontal slices in Figure 3 for olivine. First a rectangular cylinder is cut from the raw image, containing only the sample and no parts of the sample holder. Next a histogram-based segmentation is performed that segments the sample into voxels of pure air and material as well as water/ice if present. Imaging is performed in one scan each for oven-dried, drained, and saturated samples, each being 10–20 mm in height. In the absence of water, which is the case for oven-dried samples, segmentation into air and material was based on Otsu's method [41]. When water is present, this approach is not always feasible. Segmentation was then performed manually by inspection of images during variation of thresholds close to the valleys of histogram peaks, guided by the threshold obtained from oven-dried samples. For the material olivine, where absorption peaks between air, water and olivine, are well separated, this approach worked well. However, for the other two adsorbents charcoal and bark there are two complications: First, these materials show absorption coefficients closer to water and second, they contain sub-resolution micropores (responsible for unfrozen water uptake) that cannot be identified in the X-ray images. For these materials the segmentation is either more uncertain or impossible without additional information from density and unfrozen water contents.

Finally, the 3-d images have been used for numerical simulation of the saturated hydraulic conductivity. This was performed with the SimpleFFT solver of the FlowDict module in GeoDict, computing stationary fluid flow on a uniform grid based on the iterative solution of the Stokes–Brinkman equation [42]. FlowDict computes the permeability of a medium which was converted to hydraulic conductivity at $2\text{ }^\circ\text{C}$. For the simulations the dry images were used with all air voxels replaced by water voxels. Simulations were performed with 3-d images of $1200 \times 1200 \times 600$ voxels ($3 \times 3 \times 1.5\text{ cm}$) on a Dell T7910 workstation, requiring roughly 60 Gb RAM. Running on 4 cores with a 3 GHz cpu a simulation took between 10 and 20 h until an accuracy of 0.001 is obtained. To be able to simulate the present geometry of a column of height 4 times the diameter simulations were run on 2 times binned coarser resolution images (50 micrometer voxel size, $600 \times 600 \times 2400$ voxels). This decreased the permeability only by 5%. For an estimate of uncertainty of sample preparation, simulations were run for two different sand samples that were split into 5 subsamples, to obtain an overall variability of $\pm 20\%$. Recent work has demonstrated the quality of the numerical solution of the FlowDict solver in comparison to observations [43–45].

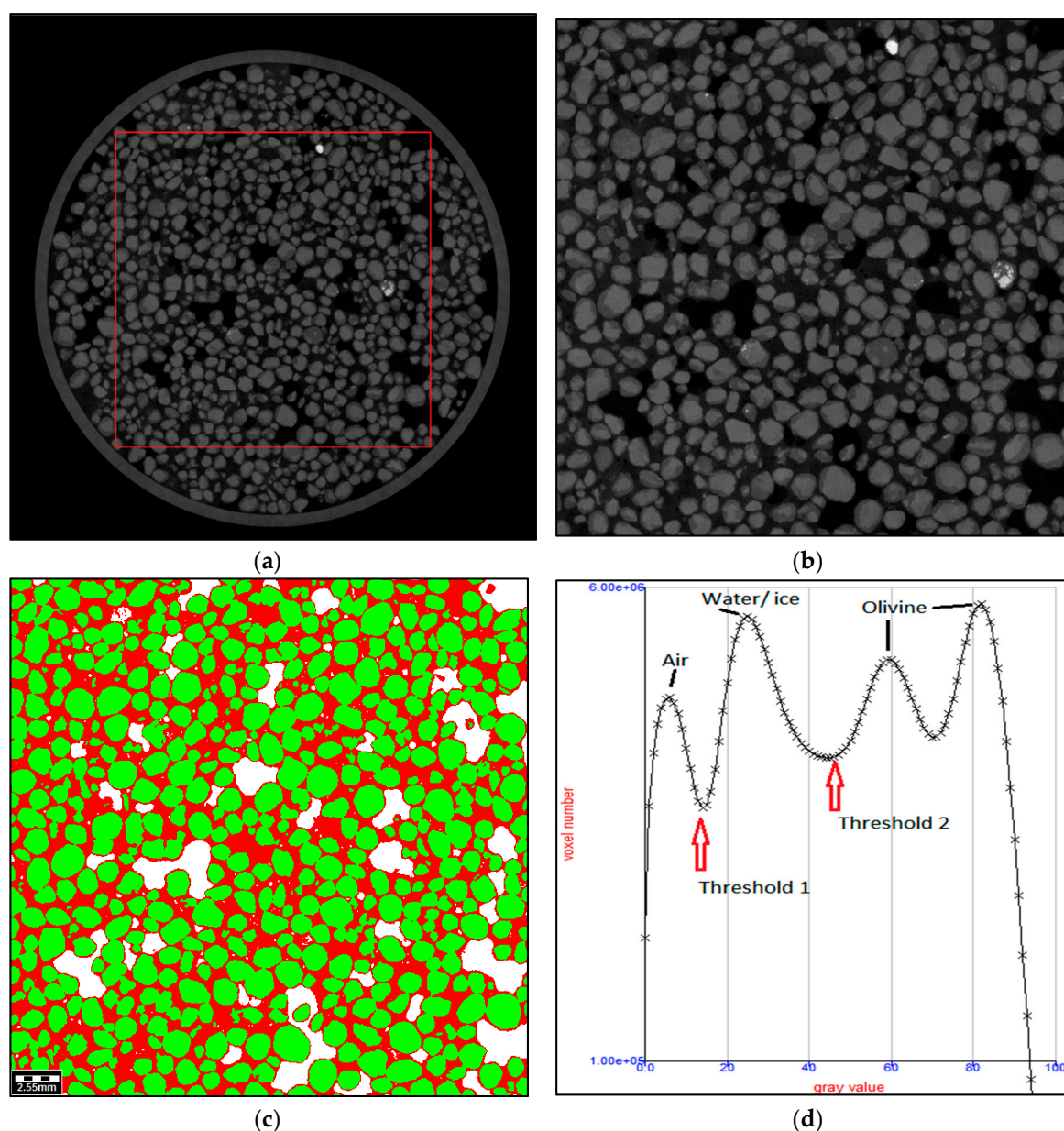


Figure 3. Schematic conversion sequence for saturated olivine from raw image (a,b) to segmented image (c), the three elements composing the sample are identified; water content is represented in red color, particle content in green color, and air in white color. (d), the X-ray absorption histogram is presented with the thresholds that split into individual elements.

3. Results and Discussion

3.1. Unfrozen Water Contents Obtained by the Contact Method

Figure 4 shows a cross plot of the gravimetric unfrozen water content, W_u , versus the temperature. The amount of unfrozen water varies from 0.11% for sand to 40.9% for charcoal, for a temperature range from 0 to -11 °C (Figure 4). The large specific surface area of charcoal (882 m²/g, obtained with Brunauer–Emmett–Teller test), and the increasingly smaller pore size within the bark [46] can explain the largest amount of unfrozen water measured in these organic materials. On the other hand, the lack of fines and micro porosity (surface area = 0.56 m²/g) of the sand (80% of SiO₂ by weight) can explain the smallest amount of unfrozen water measured in this study (Figure 4a). Presence of silt and clay fractions will lead to larger surface area by increasing the micro porosity and, consequently,

larger unfrozen water contents, as the typical soil for bio-infiltration showed (2%–2.7%). Note that the mix 1 has a slightly higher unfrozen water content compared to the sand due to the relatively low unfrozen water content present in the olivine. However, in mix 2, the amendment of sand with 5% charcoal helped to increase the unfrozen water content of the mixture by a factor of 10.

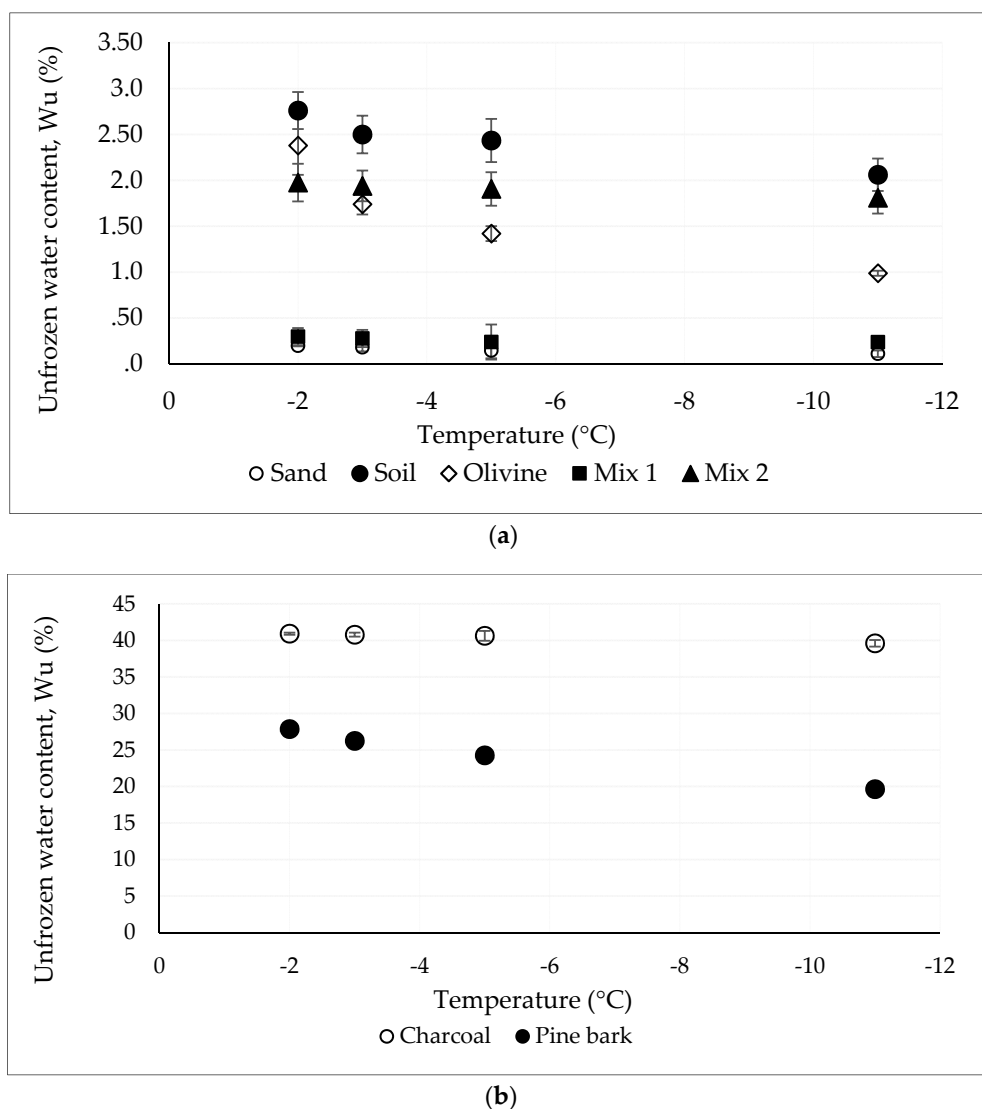


Figure 4. Gravimetric unfrozen water content with error bars of the adsorbents and sand used in this study. Mix 1 corresponds to a mixture of sand and olivine (17%). Mix 2 corresponds to a mixture of sand and charcoal (5%). In the mix samples, the ratio adsorbent/sand was kept the same as in the columns. Note the different scale of Y-axis between (a) and (b).

These results show that relatively coarse materials with large infiltration capacity (see Tables 2 and 3) also can offer simultaneously high capacity to adsorb water and pollution due to their large surface area and micro porosity.

3.2. XRT Images

Figure 5 illustrates the distribution of air, water and solids in the XRT images of oven-dried, field capacity, and saturated samples. The figure shows a horizontal slice for each material at the water content for -2.5 °C. Volume fractions of air, water and solids obtained from the three-dimensional images are given in Table 4 and discussed in the following for the different materials presented in this study.

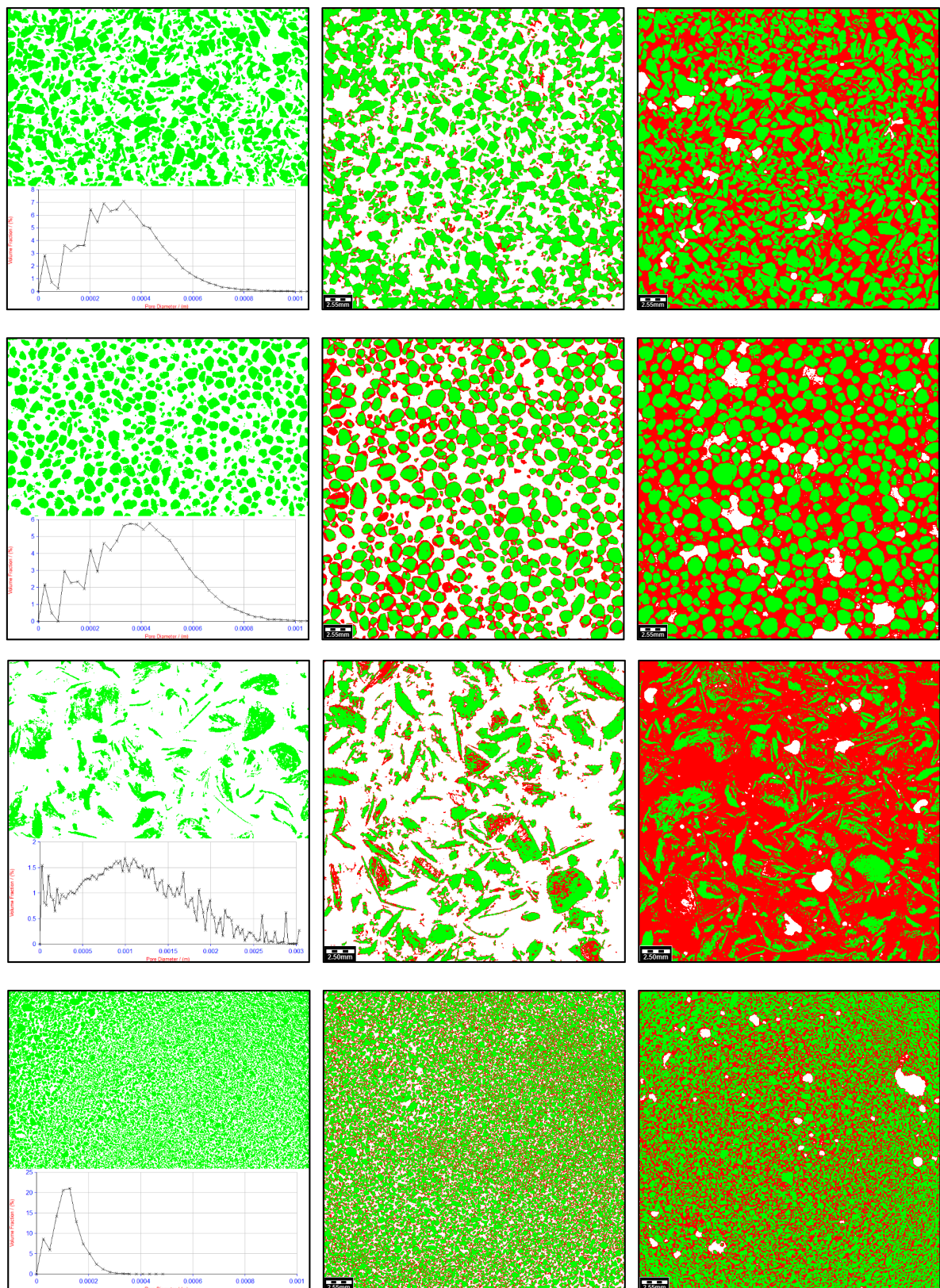


Figure 5. X-ray images of the different materials (from top to bottom) at $-2.5\text{ }^{\circ}\text{C}$ and at different moistures (from left to right). From top to bottom: Charcoal, olivine, pine bark, and sand. From left to right: Oven-dried, drained for 24 h after saturation, and saturated. Green color represents the solids, white represents the air, and red represents the water, which can be present in the ice and liquid phase. The pore size distribution from the 3-d images is included in the oven-dried images.

Table 4. Properties of samples at $-2.5\text{ }^{\circ}\text{C}$ obtained from diverse methods, i.e., contact method and X-ray tomographic (XRT). The volumetric water content obtained by XRT is assumed to be in solid phase.

Material	Unfrozen Water Content			XRT Computation at $-2.5\text{ }^{\circ}\text{C}$					
	Porosity ¹ (%)	Gravimetric ² at $-2.5\text{ }^{\circ}\text{C}$ (%)	Volumetric ³ at $-2.5\text{ }^{\circ}\text{C}$ (%)	Water Content Prior Freezing	Volumetric Air Content (%)	Volumetric Water Content (ice content) (%)	Volumetric Solid Content (%)	Microunresolved Porosity (%)	<u>Ice content</u> ⁴ / <u>Pore space</u>
Charcoal	72	41	21.7	Oven-dried	45 ± 5	0	55 ± 5	27 ± 5	-
				Field capacity Saturated	44 ± 3	5 ± 6	51 ± 5	23 ± 5	0.11
Olivine	47	1.75	3.1	Oven-dried	2.4 ± 0.4	46 ± 10	51 ± 10	23.6 ± 10	0.95
				Field capacity Saturated	44 ± 2	0	56 ± 2	3 ± 2	-
Pine bark	87	28	6.7	Oven-dried	35 ± 1	11 ± 2	53 ± 2	1 ± 2	0.26
				Field capacity Saturated	11 ± 1	34 ± 2	55 ± 2	2 ± 2	0.77
Sand	44	0.17	0.25	Oven-dried	74 ± 3	0	26 ± 3	13 ± 3	-
				Field capacity Saturated	63 ± 2	12 ± 6	25 ± 5	12 ± 5	0.16
Sand	44	0.17	0.25	Oven-dried	3 ± 1	72 ± 5	25 ± 5	12 ± 5	0.97
				Field capacity Saturated	43 ± 4	0	57 ± 4	1 ± 4	-
					26 ± 3	17 ± 5	57 ± 4	1 ± 5	0.40
					1.9 ± 0.4	41 ± 3	57 ± 4	1.1 ± 3	0.95

¹ From Table 1. ² From the contact method (see Section 3.1). ³ Volumetric content = Gravimetric content · Bulk density. ⁴ Pore space = (air + water) XRT based volumetric contents.

Charcoal has an internal porosity in addition to the porosity between the solid particles. The detectable porosity obtained from the oven-dried sample is $45 \pm 5\%$ compared to a total porosity of 72% estimated from density measurements, indicating a microunresolved porosity of $27 \pm 5\%$. This value agrees reasonably with the volumetric unfrozen water fraction of 21.7% , and suggests that this fraction of water is strongly bound to pores undetected by XRT imaging. Note that the pore size distribution indicates some unresolved porosity fraction at sizes below the smallest size class resolved (25–50 micron)

The X-ray contrast between a material and water defines how accurate the images can be segmented into water and materials (noise being always present) by choosing a threshold between the materials. Uncertainties provided in the table are obtained by 1) obtaining an automated threshold and 2) varying this threshold by a value corresponding to the noise level. This contrast is different for the materials and largest for olivine-water, with corresponding lowest uncertainties in the porosity values. Indeed, for olivine the porosity based on density measurements (47%) and XRT values ($44 \pm 2\%$) agree well, and the unresolved porosity matches the 3% unfrozen water fraction. The air content of 11% in the saturated olivine sample appears high. A closer look showed that this content does not come from air bubbles in the pore water alone, yet that the pores connect through the whole sample. It is suspected that the water was lost while placing the samples into the aluminum sample holders for XRT scanning.

Pine bark has a wide spectrum of X-ray absorption coefficients and no well-defined single peak. In the pore size histogram it is seen that the frequency of pores rises from a minimum near 200 micrometer towards smaller sizes, indicating some fraction of unresolved pores in the 0.1–25 micron regime not relevant for unfrozen water. The comparison of XRT porosity in the oven-dried sample (74%) with the value from density measurements (87%) indicates that 13% in terms of total porosity is in pores less than $25 \mu\text{m}$. Comparing this with the volumetric unfrozen water fraction of 6.7% , there is a mismatch of 6% , a value that appears not inconsistent with the noted rise in pore frequency at low pore sizes. Hence, similar as in the case of charcoal, the microunresolved porosity indicated by XRT measurements is consistent with unfrozen water measurements and also indicates the pore fraction that neither seen in XRT images nor obtained by unfrozen water adsorption.

In the case of sand, the density observation of porosity (44%) is close to the XRT imaging results ($43 \pm 4\%$). Therefore, practically no microunresolved porosity is detected. This is consistent with the well-defined maximum in the pore size distribution between 100 and 125 micron (indicating not many pores below 25 micron) as well as with the low unfrozen water fraction for sand. Additionally, in the field capacity scenario there is still 17% ice content despite the fact that the sample was allowed to drain for 24 h prior to freezing. A look at the pore size distribution indicates that sand has, compared to the other media, the largest fraction of small pores, being consistent with its apparent largest holding capacity during drainage.

3.3. Column Test

Saturated hydraulic conductivities at room temperature, $K_{20\text{ }^\circ\text{C}}$, measured in the studied filters (Tables 2 and 3) were to a great extent higher than recommended values by international guidelines for infiltration practices in temperate climates (0.003 mm/s [47], 0.007 m/s [48]). It is noteworthy that even saturated hydraulic conductivities corrected for $2\text{ }^\circ\text{C}$, $K_{2\text{ }^\circ\text{C}}$, were considerably higher than values suggested by [33] (0.03 mm/s) for bioretention in a Nordic climate, as well as the more restrictive Austrian guidelines [49] (0.1 mm/s). In the setup the adsorbents had little effect on the total saturated conductivity, i.e., a slight decrease due to the adsorbents was observed in all experiments. As hydraulic conductivities of all adsorbents are larger than for sand (see table) this is in conflict with what a simple serial hydraulic conductivity model would suggest. Potential processes that may create such behavior are (1) internal erosion with fine particles accumulating at one end of the columns, (2) packing of grains of different size, and, with regards to the setup, (3) the localized nozzle outflow in the columns. Internal erosion is probably not an issue for the medium grain size sand, when considering the criterion that more than 20% of grain mass needs to be smaller than 0.08 mm [50]. Packing of grains of different

size is well known as a factor [51]. For a concise analysis of these problems XRT imaging will be a promising approach. In this study the XRT analysis were constrained by the physical sample size, and thus were not able to analyze the large columns in this respect. However, fluid flow simulations of the hydraulic conductivity of sand were performed to investigate the effect of the outlet restriction by a nozzle (Table 5). For the geometry (nozzle diameter 6% of column diameter, height 4 times column diameter) a reduction in saturated hydraulic conductivity by a factor of 2.5 was obtained due to the outflow restriction. The reduction can be expected to increase with decrease in nozzle diameter yet to decrease with column height. Note that [52] obtained a similar reduction, yet with a larger nozzle to diameter ratio and a smaller height to diameter ratio. An interesting result in the latter study was an improved filter efficiency during restricted flow. In this study, the XRT simulations confirm the results of the column tests and demonstrate that the unrestricted saturated hydraulic permeability is slightly larger than obtained with the nozzle outflow. For future work it is proposed that XRT imaging + numerical simulations should be capable to quantify geometric effects and obtain optimal filter configurations.

Table 5. Saturated hydraulic conductivity at 2 °C (a) from column test with nozzle, (b) from numerical simulations with nozzle, and (c) from numerical simulations without nozzle.

Filter Media	Column Test with Nozzle (mm/s)	Numerical Simulation with. Nozzle (mm/s)	Numerical Simulation without Nozzle (mm/s)
Charcoal	-	-	4.3
Olivine	-	-	9.2
Pine bark	-	-	64
Sand	0.17 ± 0.01	0.23 ± 0.04	0.57 ± 0.10

For the tests under freezing temperatures, water breakthrough was achieved after 24 h from the beginning of the experiment in all cases (Tables 2 and 3). These results differ to a great extent from [23], in which every registered breakthrough was less than 10 h in columns composed of loamy sand. Another similar study performed on two engineered soils meant for bio-filtration yielded breakthrough times lower than 10 h as well [24]. Despite the fact that column dimensions between these two studies differed widely the results obtained with regard to breakthrough times were in the same range. Discrepancies found in water breakthrough values between these and our studies are explained by differences in experimental boundary conditions as well as the media used in the columns. The temperature of the infiltrating water used in the mentioned studies was +5 °C and +8–9 °C, respectively. The experiments were performed in a cold chamber at +5 °C and at room temperature, respectively. Additionally, soil moisture was adjusted to 5%–20% and 5%–10%, respectively. In the present, ponding water was adjusted to a temperature closer to actual snowmelt water temperature, i.e., +2 °C [53]. Additionally, the experiments were carried out in a cold chamber set at +2 °C, and media was tested at considerably larger water contents (full saturation and field capacity). The highest energy demand in the melting process is the latent heat of fusion of ice (334 kJ/kg), which is two orders of magnitude larger than the energy needed to increase the temperature of ice by 1 °C (2.1 kJ/kg). Hence, higher media water contents tested in this study will require a higher amount of energy to melt the ice. The heat flux in this column study is composed of conduction and advection processes. The advective heat transport into the sample is proportional to $K \cdot dT$, where K is the hydraulic conductivity and dT the temperature difference between the melting point of ice (0 °C) and the temperature of the percolating fluid. Initially and as long as infiltration is inhibited by ice, the role of K will be less pronounced and the heat transfer by conduction will dominate. Temperature of the ponding water used in this study was lower than the mentioned studies. This fact will strongly affect the heat flux and the thermal budget of the system and may explain considerably longer times to observe breakthrough. However, a more detailed study would be needed to determine how convection, conduction, boundary conditions, and soil properties influence the breakthrough time.

There was found a statistically significant difference among adsorbent placements with regard to time of water breakthrough (one-way ANOVA test at level of significance = 5%). Placement of the adsorbent underneath the sand yielded the longest time to water breakthrough of 46–55 h. Pure sand had a breakthrough time of 50 h. A possible explanation is that sand particles fall, by gravity, into the pores of the underlying filter media, creating a lower permeability layer at the bottom. When the filter media are overlying, a faster breakthrough is observed, which is expected as one would not expect mixing of the materials, implying a linear combination of breakthrough times as result. However, the shortest water breakthrough was observed for mixing the adsorbent with the sand, as observed with olivine and charcoal. A possible explanation is that the larger filter particles, when distributed homogeneously, increase the average void and pore size along the media depth (creating larger flow paths through the media already at a stage when not all of the ice has melted).

The infiltration rates measured 24 h since water breakthrough are a snapshot in time and should be interpreted as an upper bound of infiltration near steady water percolation. Interestingly, the relative infiltration rates (normalized by the saturated hydraulic conductivity at 2 °C) are positively linked with the water breakthrough (Figure 6). If breakthrough time would be controlled by infiltration rate, one would expect a negative correlation. The relationship thus points to the role of ice content: Higher breakthrough time means that more ice can be melted, in turn resulting in higher infiltration. However, future studies will need to address the temporal change in infiltration rate after breakthrough.

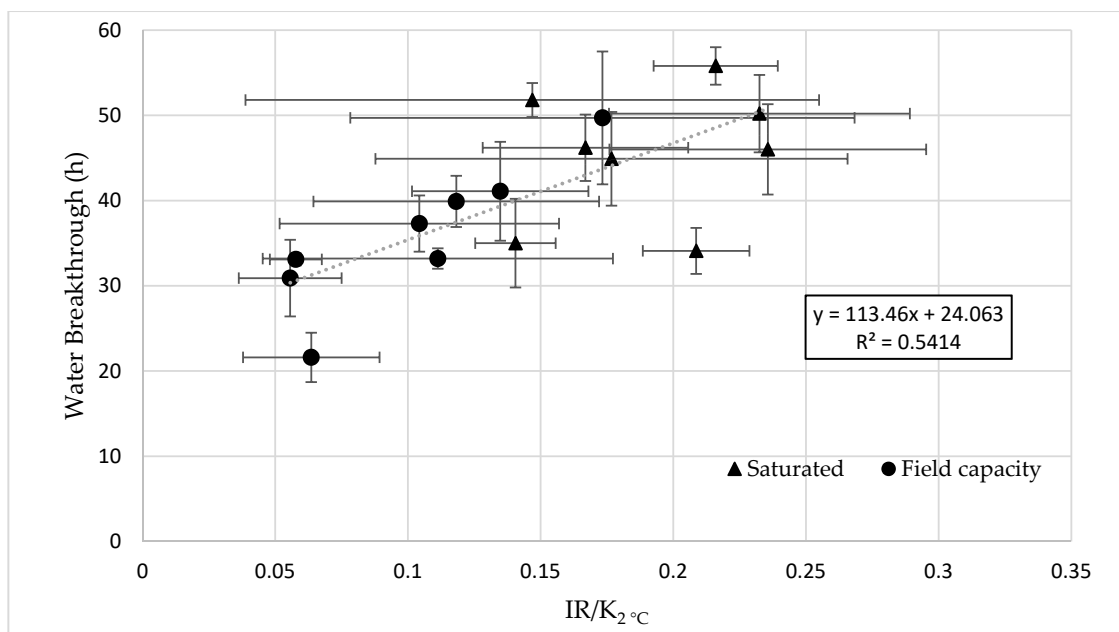


Figure 6. IR/ K₂ °C vs water breakthrough for the different column tests.

With regard to the error bounds in the results we do not observe a statistically significant difference between hydraulic infiltrations rates at saturation and at field capacity in the no freezing experiments. However, columns that drained prior freezing showed in average statistically lower (two sample t-test at level of significance = 5%) infiltration rates with regard to the saturated hydraulic conductivity at 2 °C (see at IR/ K₂ °C in Tables 2 and 3), as well as lower breakthrough time (Tables 2 and 3 and Figure 6). This is consistent as fast water breakthrough implies less heat transfer and ice melt. The lower IR/K₂ °C compared to saturated flow is expected, in general, for unsaturated samples, and also for our special case where samples drained through the bottom may not refill completely when water is poured from the top. The difference is roughly a factor 2 indicating that the drained field capacity state is behaving somewhat similar to the saturated case. Two other explanations may be noted. One possibility is the rearrangement of the particles during freezing: (at saturation downward freezing of the whole column implies strong overall expansion upon freezing, an effect that will be much less when drained

samples with less water are freezing). Another possibility is a difference flow path creation during the percolation with melting that is related to convective heat transport due to the water flow and diffusive heat flow through the side walls. These components may be different for the field capacity and saturated flows, and could have created a more localized flow path for the latter case. Hence, the pathway that ponding water might have followed may be narrow and localized, in particular due to the nozzle outflow. Moreover, for the longer breakthroughs, heat from the room could possibly have added additional energy to the process through the insulation, and enhanced ice melting. The system is complex and time-dependent. e.g., [24] distinguished an initial slow stage followed by a fast stage according to the time passed after the first outflow appeared. While the determination of the saturation dependent permeability would be a useful improvement for future studies, there are many factors that need to be addressed for full understanding. In this respect numerical simulations on real 3-d XRT images will be a very useful tool in future work. Due to the scatter in the present experiments, and their time-consuming character, one option to proceed would be numerical simulations based on the XRT images, allowing for replicate numerical experiments to study the influence of many factors and boundary conditions.

The present work should thus be understood as one step to predict the infiltration response of adsorbent amended filters under freezing and thawing conditions. Despite the infiltration detriment, adsorbent amended filters proposed in this study showed good infiltration rates even under partially frozen conditions, which confirms their suitability for stormwater management in cold climates.

Values presented in Table 4 help to understand the composition of the media in the columns as well as their inner water phase distribution. Despite of their significantly larger unfrozen water content, charcoal and pine bark showed similar volumetric water content to olivine and sand at field capacity. The unfrozen water is mostly internal to the particles or in very thin surface layers and does not contribute to fluid flow. While it is not expected to affect the fluid flow (and thus infiltration rate), one may expect that it influences the breakthrough time due to the large latent heat of water, e.g., when comparing the same material filled with unfrozen compared to frozen water, one would expect that, as unfrozen water does not need to be melted, an earlier breakthrough. However, when it comes to materials of very different microstructure, it is likely that pore-scale related effects on the convective heat flow, as well as an effective thermal diffusion, will dominate the breakthrough process. Within the general uncertainties of our study an unfrozen water effect will hardly show up for the low unfrozen water content of olivine, pine bark, and sand (less than 7% of total water content). For the relatively high unfrozen water content in charcoal (30% of total) this effect will be relevant. As the charcoal unfrozen water content to a low degree depends on temperature (Figure 4), the effect should always be a faster breakthrough than for a material with the same microstructure. Hence, the effect of unfrozen water should be included in future accurate temperature-dependent numerical predictions. However, for the focus of this present work where we have focused on comparing different materials under most typical field conditions, the effects on the fluid flow were shown to be more relevant. On the other hand, density/total porosity and XRT measurements can be linked to determine the unresolved porosity, and these values compare reasonably to the unfrozen water content. To directly compare these estimates one would have to (1) investigate the different processes that keep water unfrozen and (2) image at very high resolution. This would be something for further studies, and the present work just points into this direction.

4. Conclusions

Adsorbent amended filters for runoff treatment have been tested for infiltration performance under freezing–thawing conditions. These filters are composed of homogeneous clean sand and one adsorbent (charcoal, pine bark, or olivine).

All alternative filters proposed in this study registered discharge rates higher than the recommended values for infiltration practices, independently of the water content prior to freezing. This demonstrates that the tested media are suitable for use as adsorbent amended filters for runoff

management in cold climates. However, a more detailed study would be needed to determine how convection, conduction, boundary conditions, and soil properties influence the breakthrough time.

Mixing the adsorbent homogeneously with the sand was shown to provide the lowest water breakthrough time. Where mixing is not a practical option, adsorbents with high porosity are recommended to be placed on top of the sand layer to enlarge the potential heat exchange from the incoming runoff. However, placement of adsorbents with high porosities is not recommended in layers prone to continuous saturation and with limited contact with heat sources, which is likely to occur at the bottom of the filters. Media water content prior to freezing will influence the infiltration response of the filters; runoff needed on average an additional 10 h more to pass through a saturated media than through a drained media, which confirms the importance of a good drainage in such systems. The media that was drained prior to freezing showed a higher decrease in discharge rates compared to the saturated hydraulic conductivity at 2 °C. This is most likely related to less ice content and corresponding lower required heat input to open ice-filled pore. Other factors that may play a role are; saturation dependence of hydraulic conductivity, the outflow restriction, as well as the possibility of narrower, more localized pathways for infiltration.

Unfrozen water content and infiltration are two different processes that were not strongly linked in these experiments. However, it was found that XRT observations as well as density-based porosity and unfrozen water contents give consistent results; density based total porosity corresponds to the sum of XRT-based detectable porosity plus the microunresolved porosity (in the range of the unfrozen water content).

While the XRT at present resolution is not capable to analyze unfrozen water content, combining the methods is important when it comes to saturation-dependent properties, e.g., permeability and electric conductivity, and/or their measurement and potential simulation based on XRT images. e.g., for the same saturation of 20% a charcoal samples would likely not conduct fluid at all (as the water is in the unfrozen micropores), while an olivine sample would conduct. Consequently unfrozen water will help to estimate threshold saturation and prediction of the water retention curve as well as unsaturated conductivity. Combining XRT and unfrozen water measurements is therefore a useful approach to physically understand all aspects of soil physics.

Author Contributions: C.M.-M., T.M.M., and E.S. conceived and designed the experiments. C.M.-M. performed the column and the contact method tests and analyzed the data. S.M. performed the XRT test and analyzed the data. All the authors wrote the manuscript.

Funding: This research was funded by the National Public Road Administration of Norway and the NORWAT program (Project number 603019).

Acknowledgments: The authors wish to acknowledge the National Public Road Administration of Norway for their financial support for this project. The authors wish also to acknowledge the support of the Research Council of Norway (RCN) through funding of Microscale Interaction of Oil with Sea Ice for Detection and Environmental Risk Management in Sustainable Operations (MOSIDEO, PETROMAKS2, 243812) and the Network for evaluation of X-ray computed microtomography of snow and porous ice media (XRTOICE-NET, NANO2021, 283875). We thank Karlis Rieksts for providing tools to perform the contact method tests as well as relevant inputs about thermal properties.

Conflicts of Interest: The authors declare no conflict of interest.

References

1. Khan, U.T.; Valeo, C.; Chu, A.; van Duin, B. Bioretention cell efficacy in cold climates: Part 1—Hydrologic performance. *Can. J. Civ. Eng.* **2012**, *39*, 1210–1221. [[CrossRef](#)]
2. Muthanna, T.M.; Viklander, M.; Thorolfsson, S.T. Seasonal climatic effects on the hydrology of a rain garden. *Hydrol. Process.* **2008**, *22*, 1640–1649. [[CrossRef](#)]
3. Davis, A.P.; Stagge, J.H.; Jamil, E.; Kim, H. Hydraulic performance of grass swales for managing highway runoff. *Water Res.* **2012**, *46*, 6775–6786. [[CrossRef](#)] [[PubMed](#)]
4. Blecken, G.-T.; Marsalek, J.; Viklander, M. Laboratory Study of Stormwater Biofiltration in Low Temperatures: Total and Dissolved Metal Removals and Fates. *Water Air Soil Pollut.* **2010**, *219*, 303–317. [[CrossRef](#)]

5. Blecken, G.-T.; Zinger, Y.; Deletić, A.; Fletcher, T.D.; Hedström, A.; Viklander, M. Laboratory study on stormwater biofiltration: Nutrient and sediment removal in cold temperatures. *J. Hydrol.* **2010**, *394*, 507–514. [[CrossRef](#)]
6. Khan, U.T.; Valeo, C.; Chu, A.; van Duin, B. Bioretention cell efficacy in cold climates: Part 2—Water quality performance. *Can. J. Civ. Eng.* **2012**, *39*, 1222–1233. [[CrossRef](#)]
7. Muthanna, T.M.; Viklander, M.; Gjesdahl, N.; Thorolfsson, S.T. Heavy Metal Removal in Cold Climate Bioretention. *Water Air Soil Pollut.* **2007**, *183*, 391–402. [[CrossRef](#)]
8. Seyfried, M.S.; Murdock, M.D. Use of air permeability to estimate infiltrability of frozen soil. *J. Hydrol.* **1997**, *202*, 95–107. [[CrossRef](#)]
9. Moghadas, S.; Paus, K.; Muthanna, T.M.; Herrmann, I.; Marsalek, J.; Viklander, M. Accumulation of Traffic-Related Trace Metals in Urban Winter-Long Roadside Snowbanks. *Water Air Soil Pollut.* **2015**, *226*, 404. [[CrossRef](#)]
10. Westerlund, C.; Viklander, M. Particles and associated metals in road runoff during snowmelt and rainfall. *Sci. Total Environ.* **2006**, *362*, 143–156. [[CrossRef](#)]
11. Anderson, D.M.; Tice, A.R. Predicting unfrozen water contents in frozen soils from surface area measurements. *Highw. Res.* **1972**, *393*, 12–18.
12. Watanabe, K.; Wake, T. Measurement of unfrozen water content and relative permittivity of frozen unsaturated soil using NMR and TDR. *Cold Reg. Sci. Technol.* **2009**, *59*, 34–41. [[CrossRef](#)]
13. Bouyoucos, G. *Classification and Measurement of the Different Forms of Water in the Soil by Means of the Dilatometer Method*; Michigan State University, Agricultural Experiment Station: Clarksville, MI, USA, 1917.
14. Ershov, D.; Akimov, J.; Cheverev, V.; Kuchuckov, E. *Phase Composition of Water in Frozen Rocks*; Moscow State University: Moscow, Russian, 1978.
15. Low, P.F.; Hoekstra, P.; Anderson, D.M. Some Thermodynamic Relationships for Soils at or Below the Freezing Point: 2. Effects of Temperature and Pressure on Unfrozen Soil Water. *Water Resour. Res.* **1968**, *4*, 541–544. [[CrossRef](#)]
16. Smith, M.W.; Tice, A.R. *Measurement of the Unfrozen Water Content of Soils: Comparison of NMR and TDR Methods*; CRREL Report 88–18: Washington, DC, USA, 1988.
17. Yoshikawa, K.; Overduin, P.P. Comparing unfrozen water content measurements of frozen soil using recently developed commercial sensors. *Cold Reg. Sci. Technol.* **2005**, *42*, 250–256. [[CrossRef](#)]
18. Williams, P.J.; Smith, M.W. *The Frozen Earth*; Cambridge University Press: Cambridge, UK, 1991.
19. Andersland, O.B.; Branko, L. *Frozen Ground Engineering*; John Wiley & Sons: New Jersey, NJ, USA, 2003.
20. McCauley, C.A.; White, D.M.; Lilly, M.R.; Nyman, D.M. A comparison of hydraulic conductivities, permeabilities and infiltration rates in frozen and unfrozen soils. *Cold Reg. Sci. Technol.* **2002**, *34*, 117–125. [[CrossRef](#)]
21. Stähli, M.; Bayard, D.; Wydler, H.; Flühler, H. Snowmelt Infiltration into Alpine Soils Visualized by Dye Tracer Technique. *Arct. Antarct. Alp. Res.* **2004**, *36*, 128–135. [[CrossRef](#)]
22. Al-Houri, Z.M.; Barber, M.E.; Yonge, D.R.; Ullman, J.L.; Beutel, M.W. Impacts of frozen soils on the performance of infiltration treatment facilities. *Cold Reg. Sci. Technol.* **2009**, *59*, 51–57. [[CrossRef](#)]
23. Fach, S.; Engelhard, C.; Wittke, N.; Rauch, W. Performance of infiltration swales with regard to operation in winter times in an Alpine region. *Water Sci. Technol.* **2011**, *63*, 2658–2665. [[CrossRef](#)]
24. Moghadas, S.; Gustafsson, A.M.; Viklander, P.; Marsalek, J.; Viklander, M. Laboratory study of infiltration into two frozen engineered (sandy) soils recommended for bioretention. *Hydrol. Process.* **2016**, *30*, 1251–1264. [[CrossRef](#)]
25. Ilyas, A.; Muthanna, T.M. Assessment of upscaling potential of alternative adsorbent materials for highway stormwater treatment in cold climates. *Environ. Technol.* **2016**, *38*, 705–717. [[CrossRef](#)]
26. Monrabal-Martinez, C.; Ilyas, A.; Muthanna, M.T. Pilot Scale Testing of Adsorbent Amended Filters under High Hydraulic Loads for Highway Runoff in Cold Climates. *Water* **2017**, *9*, 230. [[CrossRef](#)]
27. ISO-17892-4. *Geotechnical Investigation and Testing—Laboratory Testing of Soil—Part 4: Determination of Particle Size Distribution*; International Organization for Standardization: Geneva, Switzerland, 2016.
28. ISO-17892-3. *Geotechnical Investigation and Testing—Laboratory Testing of Soil—Part 3: Determination of Particle Density—Pycnometer Method*; International Organization for Standardization: Geneva, Switzerland, 2015.
29. Kellogg, R.M.; Wangaard, F.F. Variation in the cell-wall density of wood. *Wood Fiber Sci.* **2007**, *1*, 180–204.

30. Mineralogy Database. Available online: <http://webmineral.com/data/Olivine.shtml#.Wa6T37JJapo/> (accessed on 30 August 2017).
31. ISO-17892-1. *Geotechnical Investigation and Testing—Laboratory Testing of Soil—Part 1: Determination of Water Content*; International Organisation for Standardisation: Geneva, Switzerland, 2014.
32. Lang, J.S.; Giron, J.J.; Hansen, A.T.; Trussell, R.R.; Hodges, W.E., Jr. Investigating filter performance as a function of the ratio of filter size to media size. *Am. Water Works Assoc.* **1993**, *85*, 122–130. [[CrossRef](#)]
33. Paus, K.; Braskerud, B. Suggestions for designing and constructing bioretention cells for a nordic climate. *J. Water Manag. Res.* **2014**, *70*, 139–150.
34. Smolczyk, U. *Geotechnical Engineering Handbook, Procedures*; John Wiley and Sons: New Jersey, NJ, USA, 2003; Volume 2.
35. Crittenden, J.C.; Trussell, R.R.; Hand, D.W.; Howe, K.J.; Tchobanoglous, G. *MWH's Water Treatment: Principles and Design*; John Wiley and Sons: New Jersey, NJ, USA, 2012.
36. Natural Resources Conservation Service Soil. Available online: https://www.nrcs.usda.gov/wps/portal/nrcs/detail/soils/survey/?cid=nrcs142p2_054167 (accessed on 14 February 2017).
37. Cnudde, V.; Boone, M.N. High-resolution X-ray computed tomography in geosciences: A review of the current technology and applications. *Earth Sci. Rev.* **2013**, *123*, 1–17. [[CrossRef](#)]
38. Desrues, J.; Viggiani, G.; Besuelle, P. *Advances in X-ray Tomography for Geomaterials*; Wiley-ISTE: London, UK, 2006.
39. Ketcham, R.A.; Carlson, W.D. Acquisition, optimization and interpretation of X-ray computed tomographic imagery: Applications to the geosciences. *Comput. Geosci.* **2001**, *27*, 381–400. [[CrossRef](#)]
40. Mees, F.; Swennen, R.; Van Geet, M.; Jacobs, P. *Applications of X-ray Computed Tomography in the Geosciences*; Special Publications; Geological Society: London, UK, 2003; Volume 215, pp. 1–6.
41. Otsu, N. A threshold selection method from gray-level histograms. *IEEE Trans. Syst. Man Cybern.* **1979**, *9*, 62–66. [[CrossRef](#)]
42. Wiegmann, A. *Computation of the Permeability of Porous Materials from Their Microstructure by FFF-Stokes*; Berichte des Fraunhofer ITWM: Kaiserslautern, Germany, 2007.
43. Gervais, P.C.; Dany, F.; Bouilloux, L.; Ricciardi, L. Simulations of filter media performances from microtomography-based computational domain. Experimental and analytical comparison. *Comput. Fluids* **2015**, *116*, 118–128. [[CrossRef](#)]
44. Gelb, L.D.; Graham, A.L.; Mertz, A.M.; Koenig, P.H. On the permeability of colloidal gels. *Phys. Fluids* **2019**, *31*, 021210. [[CrossRef](#)]
45. Zarandi, M.A.; Arroyo, S.; Pillai, K.M. Longitudinal and transverse flows in fiber tows: Evaluation of theoretical permeability models through numerical predictions and experimental measurements. *Compos. Part A Appl. Sci. Manuf.* **2019**, *119*, 73–87. [[CrossRef](#)]
46. Sparks, J.P.; Campbell, G.S.; Black, R.A. Liquid water content of wood tissue at temperatures below 0 °C. *Can. J. For. Res.* **2000**, *30*, 624–630. [[CrossRef](#)]
47. ARC. *Stormwater Management Devices: Design Guidelines Manual*; Auckland Regional Council, Stormwater/Sediment Team: Auckland, New Zealand, 2003.
48. PGC. *Prince George's County Bioretention Manual*; Environmental Services Division, Department of Environmental Resources: The Prince George's County, MD, USA, 2007.
49. ONORM-B2506-1. *Soakaways for Rain Water from Roof Gutters and Reinforced Surfaces—Application, Hydraulic Dimensioning, Construction and Operation*; Austrian Standards plus GmbH: Wien, Österreich, 2010.
50. Chapuis, R.P. Predicting the saturated hydraulic conductivity of soils: A review. *Bull. Eng. Geol. Environ.* **2012**, *71*, 401–434. [[CrossRef](#)]
51. Masch, F.D.; Denny, K.J. Grain size distribution and its effect on the permeability of unconsolidated sands. *Water Resour. Res.* **1966**, *2*, 665–677. [[CrossRef](#)]
52. Kandra, H.S.; McCarthy, D.; Fletcher, T.D.; Deletic, A. Assessment of clogging phenomena in granular filter media used for stormwater treatment. *J. Hydrol.* **2014**, *512*, 518–527. [[CrossRef](#)]
53. Jennings, K.S.; Winchell, T.S.; Livneh, B.; Molotch, N.P. Spatial variation of the rain–snow temperature threshold across the Northern Hemisphere. *Nat. Commun.* **2018**, *9*, 1148. [[CrossRef](#)] [[PubMed](#)]

